PIER Letters

(Received 26 March 2024, Accepted 27 May 2024, Scheduled 12 June 2024)

Analysis and Optimization of a Wavy Rotor FRM with Curved Stator Slots

Manru Shen, Libing Jing*, and Zeyu Min

College of Electrical Engineering and New Energy
Hubei Provincial Engineering Technology Research Center for Microgrid
China Three Gorges University, Yichang 443002, China

ABSTRACT: Flux reversal machine (FRM) belongs to the stator permanent magnet (PM) machine, which has the advantages of high reliability, high efficiency, and simple structure. However, large torque ripple and low torque density limit the development prospect of FRMs. Therefore, a wavy rotor FRM (WR-FRM) with curved stator slots is proposed, which can reduce the torque ripple while improving the average torque. The top surface of the rotor tooth consists of three sinusoidal functions, and the stator slots are constructed with a spline curve. To obtain better electromagnetic performance, the multi-objective genetic algorithm is used to optimize the FRM and the WR-FRM. Finally, the electromagnetic performances of the two machines is analyzed and compared by the finite element method. The results show that compared with the FRM, the torque generated by the unit volume of PM is increased by 36.47%, and the torque ripple is reduced by 62.7%.

1. INTRODUCTION

With the development of control theory and permanent magnet (PM) material properties, PM brushless machines have attracted widespread attention. Flux reversal machine (FRM) is part of the PM brushless machine, which has a simple structure. The topology of FRM is shown in Figure 1. The stator and rotor are made of silicon steel. The windings are installed in the stator slot, and the PMs are attached to the stator teeth surface. The construction allows for high-temperature and high-speed functioning. In addition, the machine also has the characteristics of good fault tolerance and good speed regulation performance, which is suitable for aerospace, electrically driven vehicles, and other fields [1]. However, FRM also has many disadvantages, such as large torque ripple and low torque density.

To solve these problems, a method of adding a gap between a pair of adjacent PMs is proposed in [2], which improves the waveform of the back-EMF while minimizing the torque ripple. The effect of coil pitch on harmonic components of back-EMF is analyzed to reduce torque ripple [3]. In [4, 5], cogging torque is reduced by increasing the lowest common multiple of the stator and rotor teeth. In [6], asymmetric rotor teeth are designed, and the cogging torque phase is reversed. Consequently, the cogging torque is reduced. In [7–9], spoke array and Halbach array are used in the machine, which makes the torque improve greatly. In [10], the fractional slot and integer slot machines are compared, and the integer slot overlapping winding has a higher electromagnetic torque. In [11], the toroidal winding is proposed, which can effectively improve the pitch factor to improve machine performance. In [12, 13], auxiliary teeth are added to reduce magnetic leakage and increase torque.

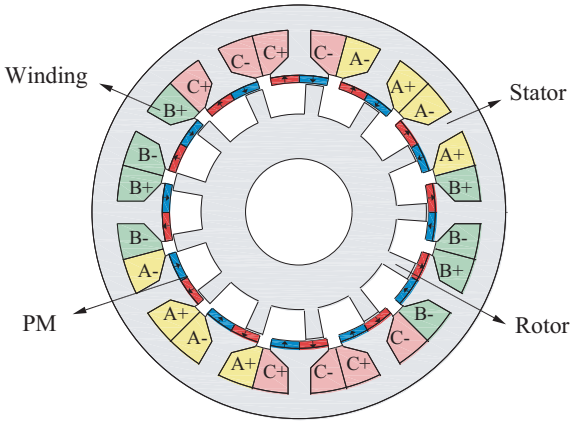

FIGURE 1. Topology of FRM.

In order to obtain torque ripple and high torque at the same time, a novel FRM is proposed in this paper. Different from the conventional FRM, the top surface of the rotor tooth is designed with three sinusoidal functions with different periods and amplitudes, which are shaped like a wave. In addition, the stator slots are composed of spline curves.

This paper has the following structure. In the second part, the topology and working principle of the WR-FRM are presented. In the third part, the wavy rotor tooth and the curved stator slot are designed and analyzed. In the fourth part, the FRM and WR-FRM are globally optimized. In the fifth part, the electromagnetic performances of the two machines are compared and analyzed. In the sixth part, the conclusion is given.

* Corresponding author: Libing Jing (jinglibing163@163.com).

2. TOPOLOGY AND WORKING PRINCIPLE

2.1. Topology

The topology of the WR-FRM is shown in Figure 2. The rotor is a simple salient pole core. The winding adopts concentrated winding, which is wound on the stator teeth. The PM surface is attached to the stator teeth. It should be noted that a curved stator slot is proposed, replacing the conventional straight stator slot. In the rotor tooth section, a wavy structure is proposed, replacing the conventional smooth teeth.

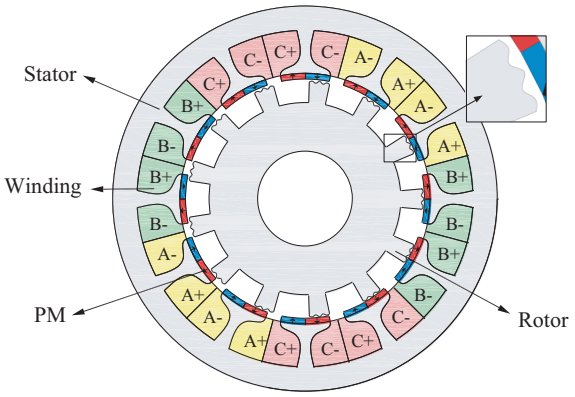

FIGURE 2. Topology of WR-FRM.

2.2. Working Principle

The working principle of WR-FRM is the same as FRM. Stable PMs produce static magnetomotive force. As the rotor teeth rotate to align with the stator teeth, the magnetic flux along the stator teeth penetrates or penetrates out the windings according to the principle of magnetic resistance. Therefore, the magnetic flux changes value and polarity as the rotor rotates. Therefore, the back-EMF is generated.

The product of the PM magnet motive force and rotor air gap permeance can be used to define the no-load air gap magnetic flux density. PM magnet motive force can be expressed as:

$$F_{PM} = \sum_{n=1,2,3,\ldots}^{\infty} F_n \cos\left(nN_{st}\theta\right) \tag{1}$$

where F_n is the Fourier coefficient when n takes $1, 2, 3\ldots$, and N_{st} is the number of stator slots. Rotor air gap permeance can be expressed as [14]:

$$\Lambda_r\left(\theta, t\right) \approx \Lambda_{r0} + \sum_{m=0,1,2,\ldots}^{\infty} \Lambda_{rm} \cos\left[mN_{rt}\left(\theta - \omega_r t\right)\right] \tag{2}$$

where Λ_{r0}, Λ_{rm} are the Fourier coefficient, and N_{rt} is the number of rotor slots. Therefore, the no-load air gap flux density can be expressed as:

$$B\left(\theta, t\right) = F_{PM}\Lambda_r\left(\theta, t\right) = \sum_{n=1,2,3,\ldots}^{\infty} F_n\Lambda_{r0} \cos\left(nN_{st}\theta\right) + \sum_{n=1,2,3,\ldots}^{\infty} \sum_{m=0,1,2,\ldots}^{\infty} \frac{F_n\Lambda_{rm}}{2}$$

$$\cos\left[\left(nN_{st} \pm mN_{rt}\right)\theta - mN_{rt}\omega_r t\right] \tag{3}$$

According to Equation (3), the harmonic pole-pair number of air gap flux density is $nN_{st} \pm mN_{rt}$, and the rotational speed of the harmonic is $mN_{rt}\omega_r/(nN_{st} \pm mN_{rt})$. The smaller modulation coefficients n and m produce the main average torque according to the principle of magnetic field modulation. Therefore, when n takes 1, 2, and m takes 0, 1, that is, N_{st}, $|N_{st} \pm N_{rt}|$, $2N_{st}$, $|2N_{st} \pm N_{rt}|$ harmonics contribute the main average torque.

3. DESIGN AND ANALYSIS OF WAVY ROTOR TOOTH AND CURVED STATOR SLOT

3.1. Wavy Rotor

The structure of the wavy rotor tooth is shown in Figure 3. The tooth top of the rotor consists of three sinusoidal functions with different periods and different amplitudes. The amplitude of the sinusoidal function in the middle is h_{bo}, and the period is $b \cdot w_{rt}$. The amplitude of the sinusoidal function on both sides is $(1-k) \cdot h_{bo}$, and the period is $(1-b) \cdot w_{rt}$. k and b are scale factors.

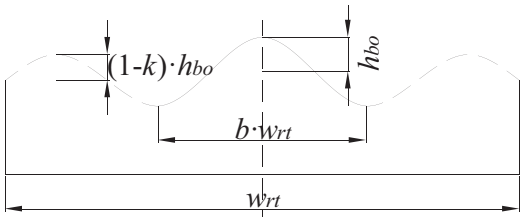

FIGURE 3. The structure of wavy rotor tooth.

h_{bo} is an important parameter related to the magnitude of the three sinusoidal wave amplitudes, which reflects the maximum length of the air gap. Other parameters of the machines remain unchanged, and only the structure of the rotor tooth surface is changed. Figure 4 shows the torque characteristics change with h_{bo}. It should be noted that $h_{bo} = 0$ represents the conventional smooth rotor tooth. When h_{bo} is 0 mm, the average torque is 20.44 N · m, and torque ripple is 4.5%. When h_{bo} is 0.2, the torque ripple is the smallest, which is 0.64%, and the torque is 19.71 N · m. The air gap length increases with the increase of h_{bo}, and the magnetic field modulation effect is weakened consequently. However, the torque reduction caused by the increase of h_{bo} is small. At the expense of 3.57% of the average torque, the torque ripple is decreased by 85.78%.

The change of k and b affects the unevenness of the air gap. k and b affect the period of the sine function. Figure 5 shows the influence of k and b on the torque ripple of the machine. With the increase of k and b, the torque ripple increases first and then decreases.

Considering the influence of k, b and h_{bo} on the torque performance, the harmonic analysis of the no-load air gap flux density is carried out. The radial and tangential air gap flux densities of the conventional smooth teeth machine and wavy teeth machine are shown in Figures 6–7. Due to the wavy rotor teeth, the equivalent air gap of the machine becomes larger, resulting in smaller working harmonics of 1st, 12th, 24th, and 25th.

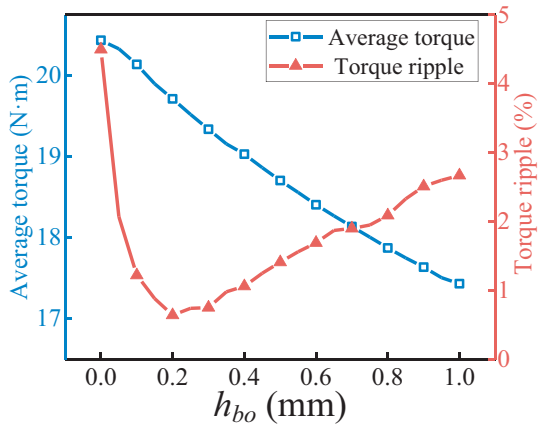

FIGURE 4. Variation of torque characteristics with h_{bo}.

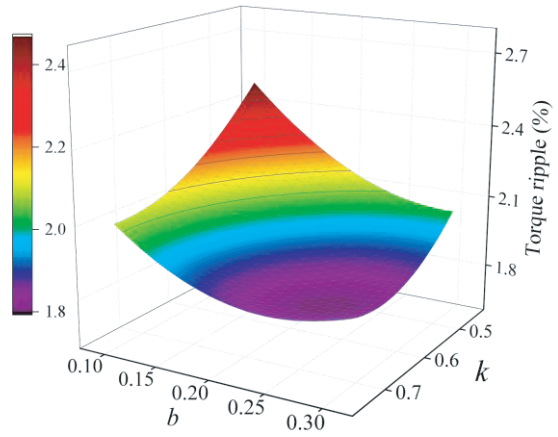

FIGURE 5. Variation of torque ripple with k and b.

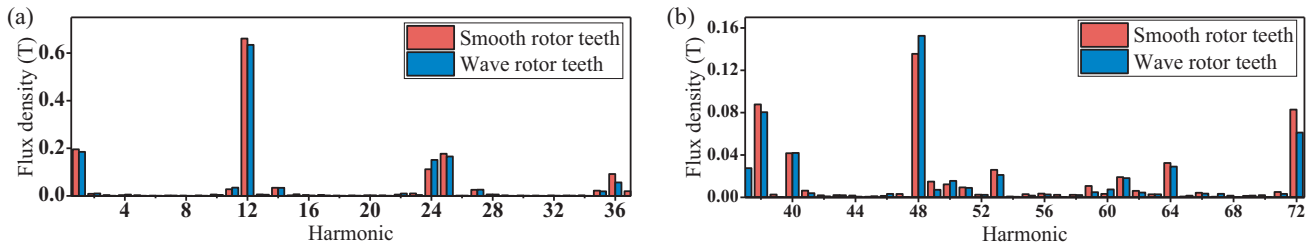

FIGURE 6. Radial flux density harmonic distribution. (a) 1–36 harmonic analysis. (b) 37–72 harmonic analysis.

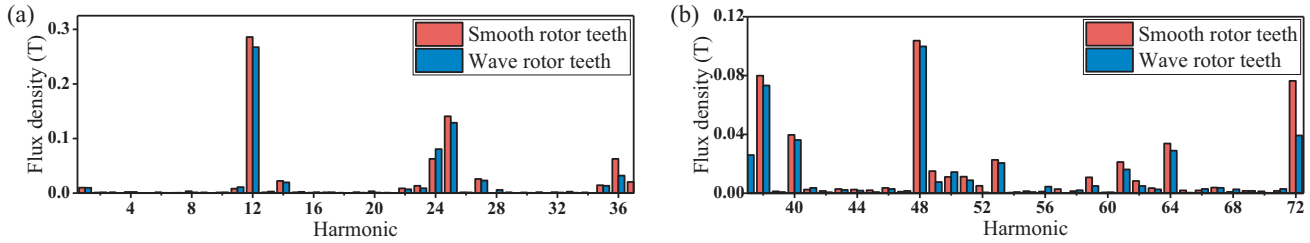

FIGURE 7. Tangential flux density harmonic distribution. (a) 1–36 harmonic analysis. (b) 37–72 harmonic analysis.

In addition to the main operating harmonics, other higher-order harmonics are suppressed. What can be observed is that the radial harmonic amplitudes of 23rd, 39th, 42nd, 44th, 47th, 57th, and 70th are close to 0, and the amplitude of the harmonics such as 38th, 41st, 49th, and 53rd are weakened to a certain extent. The amplitude change of each harmonic order in the radial direction is very similar to the amplitude change in the tangential direction. The reduction of the amplitude of the higher harmonics reduces the torque ripple. Therefore, the torque ripple is reduced.

3.2. Curved Stator Slot

The structure of the curved stator slot is shown in Figure 8. The curved stator slot is composed of spline curves composed of Point 1, Point 2, Point 3, and Point 4. Point 1 and Point 2 determine the PM width and thickness of stator pole shoe, which are the same as a conventional stator slot. It is worth noting that the parameters that determine the area of the curved stator slot are Point 3 (a_3, o_3) and Point 4 (a_4, o_4), and the parameter that determines the area of the conventional stator slot is h. The larger the slot area is, the more windings can be wound in the stator slot, which can increase the average torque.

According to the design experience of FRM, the slot fill factor of the conventional slot machine and the curved slot machine is set to 0.4 [15]. Under the condition that only the parameters of the stator slot change, curved slot machines have a higher average torque after finite element analysis. The simulation results are shown in Figure 9. The average torque of curved slot machines can reach 21.5 N · m, and the average torque of conventional slot machines is 20.03 N · m. The average torque of the curved slot can be increased by at least 7.34%.

4. GLOBAL OPTIMIZATION

In order to fairly compare the electromagnetic performance, the axial length, outer diameter, material, etc. of the two machines are the same. Table 1 shows the design parameters of the machine.

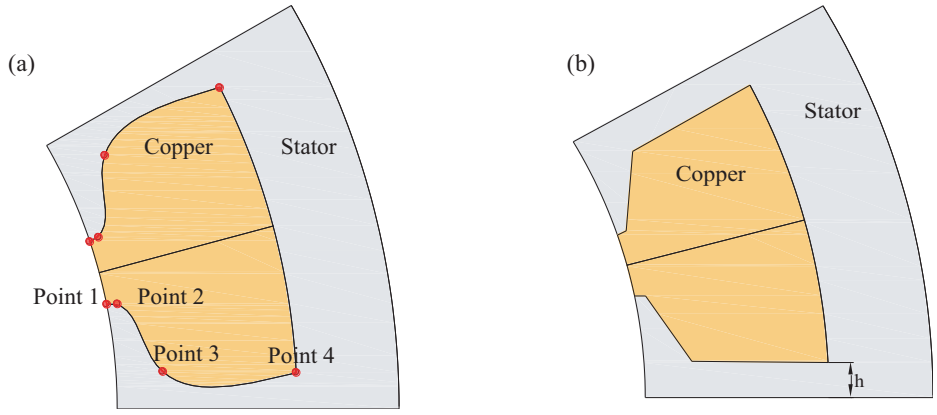

FIGURE 8. Slot structures. (a) Curved stator slot. (b) Conventional stator slot.

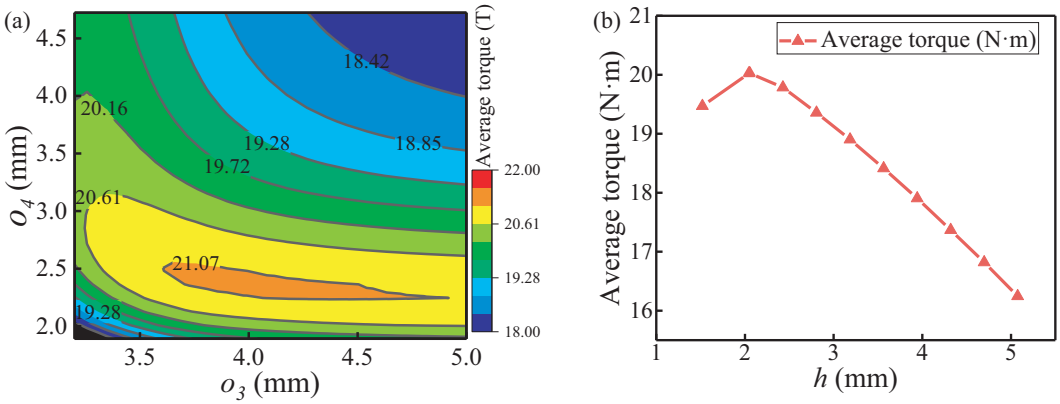

FIGURE 9. Variation of average torque. (a) Change of curved structure parameters. (b) Change of conventional structure parameters.

TABLE 1. Design parameters.

Parameters	Value
Outer radius (mm)	62
Speed (rpm)	600
Current density (A/mm^2)	9
Diameter of wire (mm^2)	1
Material of stator and rotor	DW315-50
Material of PM	NdFeB
Radius of the air gap (mm)	0.5
Axial length (mm)	120

In FRMs, r_{ry} and r_{sy} affect the saturation of the machine stator and rotor yoke. w_{rt}, h_{bo}, k, b are the relevant parameters of the rotor modulation teeth, which affect the modulation effect of the rotor on the magnetic field. r_{si} is closely related to torque. h_{PM} and w_{PM} are parameters related to PMs, which affect the excitation capacity of PM and the effective length of the air gap. h_{sh} affects the torque ripple of the machine. w_s, a_3, o_3 affect the slot area and stator tooth saturation. The above parameters affect the performance of the machine to a certain extent but are constrained geometrically. Therefore, considering the interaction between multiple parameters, the multi-objective genetic algorithm is used for global optimization.

The parametric models of the two machines are shown in Figure 10. Through the analysis and single parameter sweep in the third part, the value range of each parameter is determined and shown in Table 2. Then, the polynomial of the response surface is fitted by CCD, and the sample points are calculated in the finite element to obtain the response surface model. According to the obtained response surface model, a multi-objective genetic algorithm model is established, and the genetic algorithm is used to optimize. Finally, the optimal solution set is obtained. The optimization flowchart is shown in Figure 11.

The established optimization function is:

$$f(x_i) = \lambda \frac{f_{Tavg}(x_i)}{T_{avg0}} + \lambda_1 \frac{T_{pkavg0}}{f_{Tpkavg}(x_i)} \tag{4}$$

where T_{avg0} and T_{pkavg0} are the initial average torque and torque ripple; $f_{Tavg}(x_i)$ and $f_{Tpkavg}(x_i)$ are optimized objective functions. λ and λ_1 are the weight coefficients. The objective of optimization is to lower torque ripple while raising the average torque. Observing Equation (4), $f_{Tavg}(x_i)/T_{avg0}$ becomes larger as the optimization value $f_{Tavg}(x_i)$ becomes larger. $T_{pkavg0}/f_{Tpkavg}(x_i)$ increases with the decrease of the optimization value $f_{Tpkavg}(x_i)$. Therefore, finding the maximum value of Equation (4) can meet the design requirements. Both $f_{Tavg}(x_i)$ and $f_{Tpkavg}(x_i)$ are the objectives to be optimized by FRM and have the same importance. Therefore, the weight coefficients of both are 0.5.

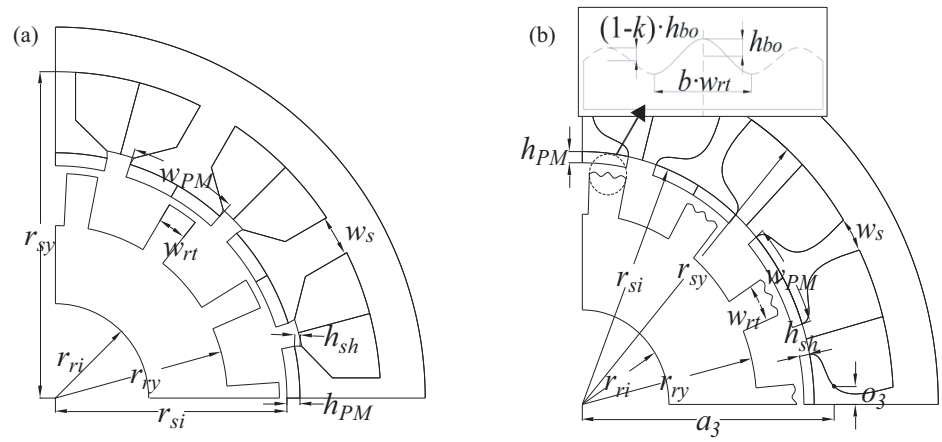

FIGURE 10. Parametric models. (a) FRM (b) WR-FRM.

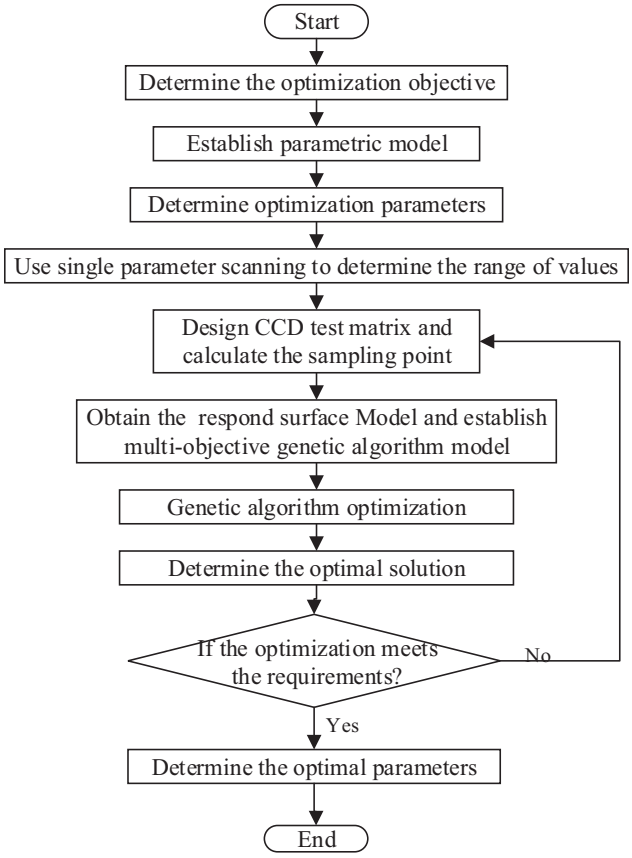

FIGURE 11. Optimization flow chart.

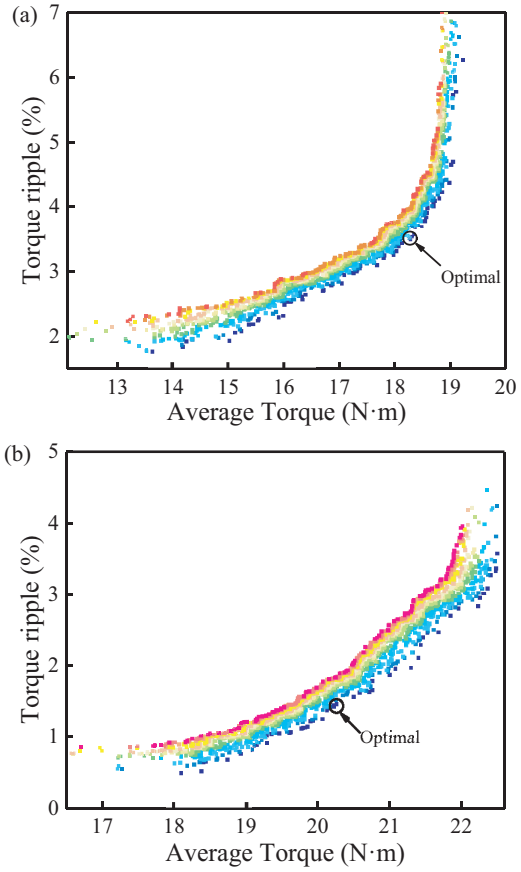

FIGURE 12. Optimization results. (a) FRM (b). WR-FRM.

The optimization results of the two machines are shown in Figure 12. It can be seen from Figure 12 that the edge of the separate point presents a curve trend. The separate blue points constitute the Pareto optimal solution set. Observing the optimal solution set of the two machines, the torque ripple of WR-FRM is always lower than that of FRM under the same torque. It can be found that the torque ripple reaches 7% when the FRM is 19.5 N · m. When the WR-FRM is 19.5 N · m, the torque ripple is less than 1%. Therefore, the torque characteristics of WR-FRM are due to FRM. Considering the torque and torque ripple, the optimization points selected are shown in Figure 12.

5. COMPARISON OF ELECTROMAGNETIC PROPERTIES

5.1. Air Gap Flux Density

Figure 13 shows the air gap flux density of the two machines. The air gap flux density amplitude of WR-FRM is 1.09 T, while the FRM air gap flux density reaches 1.21 T. Compared with the FRM, the amount of PM used in the WR-FRM is reduced by 20.6%. Consequently, the air gap flux density amplitude of the WR-FRM is reduced. The reduction of the air gap flux density amplitude can alleviate the saturation of the stator and rotor teeth. The working harmonics of both machines are

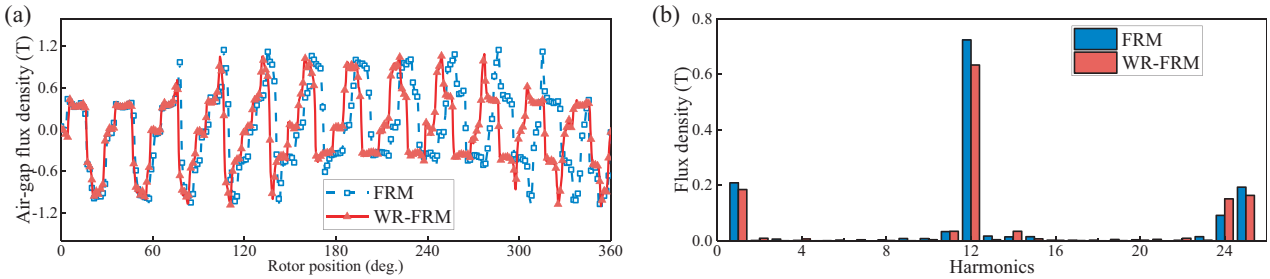

FIGURE 13. Air gap flux density. (a) Air gap flux density distribution. (b) Harmonic spectra.

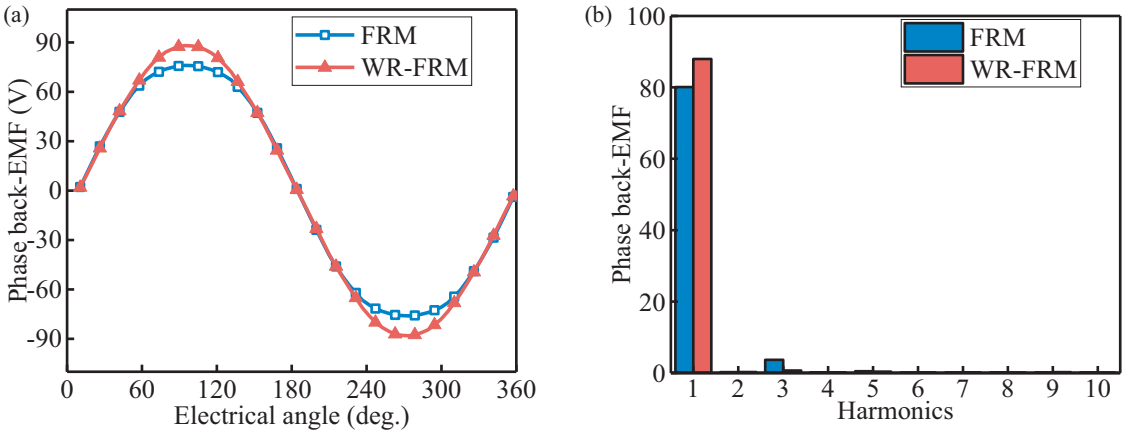

FIGURE 14. Phase back-EMF. (a) Waveform. (b) Harmonic spectra.

TABLE 2. Range and the final value of parameters.

Parameters	Range	FRM	WR-FRM
Inner radius of rotor yoke r_{ri} (mm)	13–17	14.9	15.4
Outer radius of rotor yoke r_{ry} (mm)	27–33	29	31
Inner radius of stator r_{si} (mm)	38–43	42	40.4
Inner radius of stator yoke r_{sy} (mm)	52–56	55.4	54.2
Width of rotor teeth w_{rt} (deg.)	7.5–9.5	8.4	7.6
Width of stator teeth w_s (deg.)	4–12	10.6	5.8
Width of PM w_{PM} (deg.)	20–25	24.8	23
Thickness of PM h_{PM} (mm)	1.5–2.5	2	1.8
Ordinate of point 3 o_3 (mm)	2.5–5	/	4
Abscissa of point 2 a_3 (mm)	42–47	/	43
Amplitude of wave rotor h_{bo} (mm)	0.1-0.5	/	0.1
Amplitude ratio coefficient k	0.4–0.8	/	0.5
Period ratio coefficient b	0.1–0.3	/	0.2

1st, 12th, 24th, and 25th. The working harmonic amplitude is reduced to a certain extent due to the decrease of the magnetomotive force and the increase of the effective length of the air gap.

5.2. No-Load BackEMF

Figure 14 shows the no-load back-EMF of the two machines. The no-load back-EMF amplitude of the WR-FRPM is 88.32 V, which is 15.94% higher than that of the FRM. This is because the curved stator slot can accommodate more coils. The no-load back-EMF harmonics of the two machines are shown in Figure 14(b). The back EMF waveform distortion rate can be expressed as:

$$THD = \frac{\sqrt{\sum_{i=2}^{n} B_{\delta i}^2}}{B_{\delta 1}} \times 100\% \tag{5}$$

The fundamental amplitude of the FRM is larger than that of the FRM, and the 3rd harmonic is very small. The back-EMF waveform aberration rate of the WR-FRM is 2.18%.

5.3. Torque

Figure 15 shows the torque characteristics of the two machines. Due to the wavy rotor structure, high-order harmonics are suppressed. Consequently, the torque ripple is reduced by 62.7%. Due to the expansion of the stator slot area, the torque of the WR-FRM is increased by 8.53%. It is worth noting that the PM consumption of the WR-FRM is reduced by 1/5. Therefore, it is necessary to compare the torque generated by the unit volume of PM. Table 3 lists the relevant parameter values. The torque generated by the unit PM volume of the WR-FRM is much higher than that of the FRM. In addition, the volumes of the two machines are the same, and the torque density of WR-FRM is 13.86 kN · m/m^3, which is 8.54% higher than that of FRM. Therefore, the WR-FRM has greater competitiveness.

5.4. Losses and Efficiency

Figure 16 shows a comparison of the loss components of the two machines at rated currents. After finite element analysis, the core loss

TABLE 3. Torque characteristics and PM volume.

	FRM	WR-FRM
Average torque (N · m)	18.52	20.1
Torque ripple (%)	3.11	1.16
Unit volume of PM (m^3)	5.11e-5	4.06e-5
Torque generated by the unit volume of PM (kN · m/m^3)	362.08	494.03
Torque density (kN · m/m^3)	12.77	13.86

TABLE 4. Loss components and efficiency.

	FRM	WR-FRM
Core loss p_{core} (W)	27.46	26.84
PM loss p_{PM} (W)	6.5	4.5
Copper loss p_{cu} (W)	61.24	79.7
Output power P_{em} (W)	1163.65	1262.92
Efficiency η	92.44%	91.92%

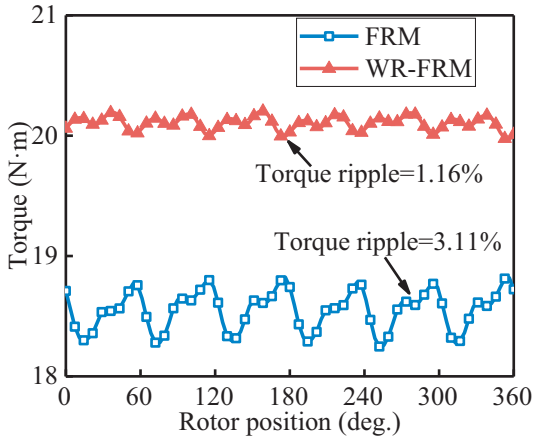

FIGURE 15. Torque characteristics.

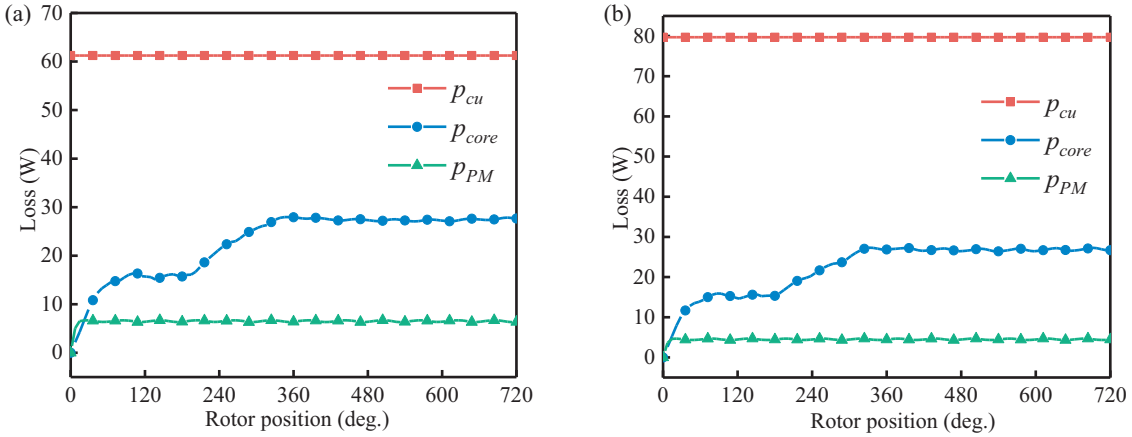

FIGURE 16. Comparison of main losses. (a) FRM. (b) WR-FRM.

and PM loss of the two machines are similar. The largest difference is copper loss, which is mainly due to the installation of more windings in the WR-FRM.

The efficiency of the machine is calculated as:

$$\eta = P_{em}/(P_{em} + p_{core} + p_{PM} + p_{cu}) \tag{6}$$

Although the output power of the WR-FRM is larger, the efficiency of the WR-FRM is slightly lower than that of the FRM due to the large copper loss of the WR-FRM. Table 4 lists the loss components and efficiency.

6. CONCLUSION

In this paper, a wavy rotor FRM with curved stator slots is proposed and analyzed from the working principle, key parameter analysis, global optimization, and comparison of the electromagnetic performance of the FRM. Some of the findings and discussions are summarized below:

1) When only the shape of the rotor tooth surface is changed, the wavy rotor machine sacrifices 3.57% of the average torque compared to the smooth rotor machine, and the torque ripple can be reduced by 85.78%.
2) When only the shape of the stator slot is changed, the curved slot can be increased by at least 7.34% compared with the conventional straight slot.
3) Compared with conventional FRM, the proposed WR-FRM can provide a 15.94% increase in back EMF, an 8.53% increase in average torque, a 62.7% reduction in torque ripple, and a 36.47% increase in torque generated by the unit volume of PM. Therefore, WR-FRM has better competitiveness.

REFERENCES

[1] Gao, Y., R. Qu, D. Li, and J. Li, "Torque performance analysis of three-phase flux reversal machines," *IEEE Transactions on Industry Applications*, Vol. 53, No. 3, 2110–2119, May-Jun. 2017.

[2] Zhu, X. and W. Hua, "An improved configuration for cogging torque reduction in flux-reversal permanent magnet machines," *IEEE Transactions on Magnetics*, Vol. 53, No. 6, 1–4, Jun. 2017.

[3] Hua, W., X. Zhu, and Z. Wu, "Influence of coil pitch and stator-slot/rotor-pole combination on back EMF harmonics in flux-reversal permanent magnet machines," *IEEE Transactions on Energy Conversion*, Vol. 33, No. 3, 1330–1341, Sep. 2018.

[4] Zhao, Y., B. Kou, and X. Zhao, "A study of torque characteristics of a novel flux reversal machine," in *2019 22nd International Conference on Electrical Machines and Systems (ICEMS)*, 1–5, 2019.

[5] Hao, L., M. Lin, D. Xu, N. Li, and W. Zhang, "Cogging torque reduction of axial-field flux-switching permanent magnet machine by rotor tooth notching," *IEEE Transactions on Magnetics*, Vol. 51, No. 11, 1–4, Nov. 2015.

[6] Kim, T. H., S. H. Won, K. Bong, and J. Lee, "Reduction of cogging torque in flux-reversal machine by rotor teeth pairing," *IEEE Transactions on Magnetics*, Vol. 41, No. 10, 3964–3966, Oct. 2005.

[7] Qu, H. and Z. Q. Zhu, "Analysis of spoke array permanent magnet flux reversal machines," *IEEE Transactions on Energy Conversion*, Vol. 35, No. 3, 1688–1696, Sep. 2020.

[8] Xie, K., D. Li, R. Qu, Z. Yu, Y. Gao, and Y. Pan, "Analysis of a flux reversal machine with quasi-halbach magnets in stator slot opening," *IEEE Transactions on Industry Applications*, Vol. 55, No. 2, 1250–1260, Mar.-Apr. 2019.

[9] Jing, L., W. Tang, T. Wang, T. Ben, and R. Qu, "Performance analysis of magnetically geared permanent magnet brushless motor for hybrid electric vehicles," *IEEE Transactions on Transportation Electrification*, Vol. 8, No. 2, 2874–2883, Jun. 2022.

[10] Wu, Z. Z., Z. Q. Zhu, and H. L. Zhan, "Comparative analysis of partitioned stator flux reversal pm machines having fractional-slot nonoverlapping and integer-slot overlapping windings," *IEEE Transactions on Energy Conversion*, Vol. 31, No. 2, 776–788, Jun. 2016.

[11] Li, H., Z.-Q. Zhu, and H. Hua, "Comparative analysis of flux reversal permanent magnet machines with toroidal and concentrated windings," *IEEE Transactions on Industrial Electronics*, Vol. 67, No. 7, 5278–5290, Jul. 2020.

[12] Yang, H., H. Lin, Z.-Q. Zhu, S. Lyu, and Y. Liu, "Design and analysis of novel asymmetric-stator-pole flux reversal PM machine," *IEEE Transactions on Industrial Electronics*, Vol. 67, No. 1, 101–114, Jan. 2020.

[13] Jing, L., T. Wang, W. Tang, W. Liu, and R. Qu, "Characteristic analysis of the magnetic variable speed diesel-electric hybrid motor with auxiliary teeth for ship propulsion," *IEEE/ASME Transactions on Mechatronics*, Vol. 29, No. 1, 668–678, Feb. 2024.

[14] Zhu, X., W. Hua, W. Wang, and W. Huang, "Analysis of back-EMF in flux-reversal permanent magnet machines by air gap field modulation theory," *IEEE Transactions on Industrial Electronics*, Vol. 66, No. 5, 3344–3355, May 2019.

[15] Zhu, X. and W. Hua, "Stator-slot/rotor-pole pair combinations of flux-reversal permanent magnet machine," *IEEE Transactions on Industrial Electronics*, Vol. 66, No. 9, 6799–6810, Sep. 2019.